



Full length article

Simulated diffusion spreadability for characterizing the structure and transport properties of two-phase materials

M. Skolnick^a, S. Torquato^{a,b,c,d,e,*}^a Department of Chemistry, Princeton University, Princeton, NJ, 08544, USA^b Department of Physics, Princeton University, Princeton, NJ, 08544, USA^c Princeton Institute of Materials, Princeton University, Princeton, NJ, 08544, USA^d Program in Applied and Computational Mathematics, Princeton University, Princeton, NJ, 08544, USA^e School of Natural Sciences, The Institute for Advanced Study, Princeton, NJ, 08540, USA

ARTICLE INFO

Keywords:

Hyperuniformity
Heterogeneous materials
Diffusion spreadability
Inhomogeneous diffusion

ABSTRACT

Time-dependent diffusion processes between phases of heterogeneous materials are ubiquitous in a variety of contexts in the physical, chemical, and biological sciences. Examples of such materials include composites, porous materials, geological media, cellular solids, polymer blends, colloids, gels, and biological media. The recently developed diffusion spreadability, $S(t)$, provides a direct link between time-dependent interphase diffusive transport and the microstructure of two-phase materials across length scales (Torquato, 2021); thus making $S(t)$ a powerful dynamic means for classifying all statistically homogeneous microstructures, spanning from anti-hyperuniform to hyperuniform. It was shown that the small-, intermediate-, and long-time behaviors of $S(t)$ are directly determined by the small-, intermediate-, and large-scale structural features of the material. Moreover, the spreadability can be applied as a physical-property based tool for microstructural characterization in the absence of or as supplement to scattering information. In this work, we develop a computationally efficient algorithm for ascertaining $S(t)$ directly from digitized representations of material microstructures via random-walk techniques. Our algorithm yields the time-dependent local walker concentration field $c(\mathbf{x}, t)$, a quantity not previously examined in the context of the spreadability, enabling us to compute the entropy production rate $\dot{s}(t)$ of the associated diffusion process, which is a quantity related to the rate of energy dissipation. We also derive exact analytical expressions for $\dot{s}(t)$, and find that hyperuniform materials have smaller dissipation than any nonhyperuniform materials. Lastly, we use our algorithm to compute, for the first time, the more general case of the spreadability in which the phase diffusion coefficients are distinct and provide a method for extracting the effective diffusion coefficient of the two-phase material from such data. We apply our algorithm to a variety of two- and three-dimensional simulated model (non)hyperuniform microstructures to assess their large-scale structures and diffusion properties. Given previously identified connections between the spreadability and certain nuclear magnetic resonance (NMR) and magnetic resonance imaging (MRI) procedures, our algorithm is also pertinent to such experimental studies. Overall, our algorithm has practical use in the discovery and design of heterogeneous materials with desirable time-dependent diffusion properties.

1. Introduction

Time-dependent diffusion processes in multiphase heterogeneous materials arise in a multitude of physical, chemical, and biological contexts, including material design [1–3], magnetic resonance imaging [4], surface catalysis [1,5], cell-behavior modeling [6] and controlled drug delivery [7]. Such heterogeneous materials are ubiquitous in natural and synthetic contexts, including composites, porous materials, geological media, cellular solids, polymer systems, colloids, gels, and biological media [1,2,8–13].

The diffusion spreadability, introduced by Torquato [14], is a dynamical probe that directly links the time-dependent diffusive transport with the microstructure of heterogeneous materials across length scales. The spreadability specifically considers the time-dependent problem of mass transfer of a solute in a two-phase material where all solute is initially concentrated in phase 2, and the solute has the same diffusion coefficient D in each phase. The spreadability $S(t)$ is therefore defined as the total solute present in phase 1 at time t . For two

* Corresponding author at: Department of Chemistry, Princeton University, Princeton, NJ, 08544, USA.

E-mail address: torquato@electron.princeton.edu (S. Torquato).<https://doi.org/10.1016/j.actamat.2023.118857>

Received 29 December 2022; Accepted 10 March 2023

Available online 17 March 2023

1359-6454/Crown Copyright © 2023 Published by Elsevier Ltd on behalf of Acta Materialia Inc. All rights reserved.

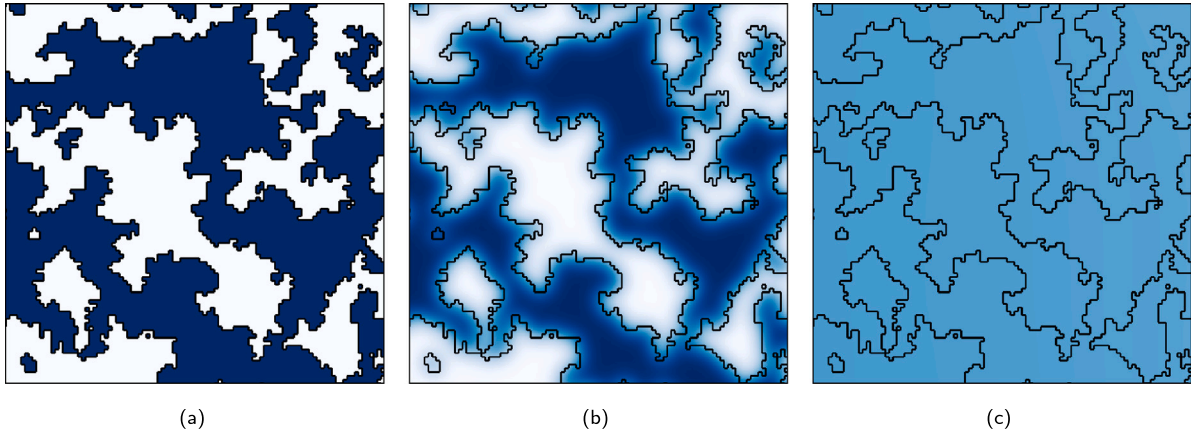


Fig. 1. This schematic depicts the concentration field for the diffusion spreadability process at different times for an amorphous two-phase material in 2D. The left panel (a) shows the uniform concentration of the solute species within phase 2 (dark blue) at time $t = 0$. The central panel (b) depicts the spreading of solute at short times. The right panel (c) depicts the uniform concentration of the solute species throughout both phases (pale blue) in the infinite-time limit. The phase interface is highlighted in black in all three panels. (For interpretation of the references to color in this figure legend, the reader is referred to the web version of this article.)

Source: This figure is adapted from Fig. 1 in Ref. [14].

different microstructures at some time t , the one with the larger value of $S(t)$ spreads diffusion information more rapidly [14]. See Fig. 1 for a schematic illustrating the spreadability phenomena for an amorphous microstructure. Expanding upon original work by Prager [15], Torquato demonstrated that $S(t)$ in any d -dimensional Euclidean space \mathbb{R}^d is *exactly* related to the microstructure via the direct space autocovariance function $\chi_V(\mathbf{r})$, or equivalently, via the spectral density $\tilde{\chi}_V(\mathbf{k})$ in Fourier space [14]:

$$\begin{aligned} S(\infty) - S(t) &= \frac{1}{(4\pi Dt)^{d/2} \phi_2} \int_{\mathbb{R}^d} \chi_V(\mathbf{r}) \exp[-r^2/(4Dt)] d\mathbf{r} \\ &= \frac{1}{(2\pi)^d \phi_2} \int_{\mathbb{R}^d} \tilde{\chi}_V(\mathbf{k}) \exp[-k^2 Dt] d\mathbf{k}. \end{aligned} \quad (1)$$

Here, ϕ_2 is the volume fraction of phase 2, $S(\infty) = \phi_1$ is the infinite-time limit of $S(t)$, and $S(\infty) - S(t)$ is called the excess spreadability.

Eq. (1) is a rare example of transport in two-phase random materials which is exactly described by only the first two correlation functions, namely, ϕ_1 and two-point statistics via either $\chi_V(\mathbf{r})$ or $\tilde{\chi}_V(\mathbf{k})$. In contrast, the preponderance of effective transport properties of random heterogeneous materials are fully determined by an *infinite* set of correlation functions to be described completely [1,16,17]. From Eq. (1), Torquato [14] demonstrated that the small-, intermediate-, and long-time behaviors of $S(t)$ are directly determined by the small-, intermediate-, and large-scale structural features of the two-phase material. Therefore, the spreadability is a powerful dynamic figure of merit to probe and categorize all translationally invariant two-phase microstructures that span from hyperuniform [18,19] to nonhyperuniform materials across length scales. These properties enable the application of the spreadability as a physical property-based tool for rigorous microstructural quantification in the absence of scattering information.

Hyperuniformity generalizes the established notions of long-range order manifested in crystals and quasicrystals to include certain exotic disordered materials. Disordered hyperuniform materials are receiving considerable attention [20–37] because they are characterized by an anomalous suppression of volume-fraction fluctuations relative to garden-variety disordered nonhyperuniform materials [18,19,38]. Since disordered hyperuniform two-phase materials are states of matter that lie between a crystal and a typical liquid, they can be endowed with novel physical properties that are directionally independent and robust with respect to defects [38]. Some notable examples include isotropic photonic and phononic bandgap materials [39–43], multifunctional materials [17,44–47], special optical and lasing materials [48–53], conductive disordered two-dimensional materials [33,54], as well

as materials with optimal transport [55,56] and mechanical properties [57]. The reader is referred to Refs. [38,47] for comprehensive reviews on hyperuniformity and hyperuniform materials.

For statistically homogeneous microstructures whose spectral densities exhibit the following power-law form

$$\tilde{\chi}_V(\mathbf{k}) \sim B|\mathbf{k}|^\alpha \quad (2)$$

in the limit $|\mathbf{k}| \rightarrow 0$, Torquato [14] showed that the long-time excess spreadability for two-phase materials in \mathbb{R}^d is given by the inverse power-law

$$S(\infty) - S(t) \sim \frac{B\Gamma[(d+\alpha)/2]\phi_2}{2^d \pi^{d/2} \Gamma(d/2)(Dt/a^2)^{(d+\alpha)/2}}. \quad (3)$$

where a is a characteristic heterogeneity length-scale and B is a microstructure-dependent coefficient. This power-law holds except for instances where $\alpha \rightarrow +\infty$, which, roughly speaking, may be regarded to correspond to stealthy hyperuniform materials (see Section 2.2 for terminology) whose excess spreadability decays exponentially fast [14], i.e.,

$$S(\infty) - S(t) \sim C e^{-\varphi t} / t \quad (\text{disordered stealthy}) \quad (4a)$$

$$S(\infty) - S(t) \sim C e^{-\varphi t} \quad (\text{ordered stealthy}) \quad (4b)$$

where C and φ are microstructure dependent parameters.

Thus, the long-time asymptotic scalings (3) and (4) for the excess spreadability can be used as a simple yet robust tool to identify and organize different hyperuniform and nonhyperuniform materials by quantifying their values of the spectral density exponent α ; see Section 2.2. We see from Eq. (3) that antihyperuniform materials ($-d < \alpha < 0$) exhibit the most slowly decaying excess spreadability $S(\infty) - S(t)$. Typical nonhyperuniform materials ($\alpha = 0$) have intermediate power-law decay rates, while those for non-stealthy hyperuniform materials ($0 < \alpha < \infty$) have the fastest decay rates among power-law cases; see Eq. (3). Eqs. (4a) and (4b) reveal that stealthy materials have excess spreadabilities that decay exponentially fast and hence possess the fastest decay rates among all statistically homogeneous systems.

Torquato [14] also identified precise mappings between the long-time asymptotic formulas for the spreadability and the nuclear magnetic resonance (NMR) pulsed field gradient spin-echo (PFGSE) amplitude [58,59] as well as diffusion magnetic resonance imaging (MRI) measurements [60]. Through such maps, one can readily translate the analysis of long-time behaviors of $S(t)$ into corresponding analyses of NMR or MRI data; enabling one to extract large-scale microstructural information of real heterogeneous materials from diffusion experiments alone—a particularly important functionality when scattering

information is unobtainable. Additionally, recent work has used the spreadability to structurally characterize a wide-variety of ordered and disordered microstructures [61,62]. In summary, the spreadability is a powerful diagnostic of microstructure in both experimental and computer-simulation scenarios. Moreover, the spreadability can be utilized as a computational tool to aid in the design and discovery of novel hyperuniform and nonhyperuniform materials with desirable physical properties, as detailed in Section 7.

In this work, we greatly expand the utility of the spreadability as a diagnostic probe of microstructure by obtaining it directly from computationally efficient random walk simulation methods.¹ We specifically develop a simulation protocol that employs trillions of lattice-bound discrete time random walkers to accurately and efficiently capture the time-dependent diffusion phenomena associated with the spreadability (see Section 4 for algorithmic details). We apply our simulation method, which we refer to as the lattice diffusion algorithm (LDA), to a variety of disordered model microstructures with varying degrees of order/disorder at different length scales (see Section 3 for details), and demonstrate that it provides a novel way to directly assess the (non)hyperuniformity of a two-phase material directly from diffusion measurements. Additionally, we use the time-dependent local concentration field $c(\mathbf{x}, t)$ to compute the specific entropy production rate $\dot{s}(t)$ of the diffusion process associated with the spreadability (see Section 5). We also derive exact analytical expressions for $\dot{s}(t)$ and show that it depends on only one-, two-, and three-point correlation functions. As one might expect, we find that the entropy production rates of hyperuniform materials decay more rapidly than those of non-hyperuniform materials, with $\dot{s}(t)$ decaying the most rapidly for stealthy systems. We also find that the rank orderings of the disordered model microstructures based on their long-time asymptotic spreadabilities and entropy production rates are consistent with one another, despite the latter incorporating additional three-point correlation function information.

The flexibility of our simulation method enables us to also compute, for the first time, the more physically realistic case of the spreadability in which phase 1 and 2 have contrasting solute diffusion coefficients [14]. Using a mapping observed by Torquato that relates the NMR PFGSE amplitude to the spreadability [14], we are able to compute the effective (homogenized) diffusion coefficient of the corresponding two-phase material in addition to its value of the exponent α . We demonstrate that our simulation results are consistent with those produced using the commercial finite element software COMSOL Multiphysics®. Our method can be readily applied using imaging data gathered in the laboratory via microscope or tomography experiments [1,63–66] since it is designed to operate on pixelized/voxelized representations of the microstructure. The method leverages Graphics Processing Units (GPUs) for massive parallelism, enabling the computationally efficient assessment of structures with $\mathcal{O}(10^9)$ pixels/voxels using $\mathcal{O}(10^{12})$ walkers.

The paper is organized as follows: in Section 2, we introduce key concepts and definitions. In Section 3, the model two-phase microstructures are described. Section 4 covers the algorithmic details of our simulation method. Exact analytical expressions for the entropy production rate are provided in Section 5. The main results of the paper are presented in Section 6. Conclusions and future research directions are discussed in Section 7.

2. Definitions and preliminaries

In this section, we introduce key concepts and definitions needed to describe two-phase microstructures; including correlation functions, and the classification of hyperuniform and nonhyperuniform materials.

¹ Currently, $S(t)$ may only be computed through autocovariance or spectral density data via Eq. (1).

2.1. Correlation functions

The microstructure of a random multi-phase material is uniquely determined by the indicator functions $\mathcal{I}^{(i)}(\mathbf{x})$ for the individual phases which are defined as

$$\mathcal{I}^{(i)}(\mathbf{x}) = \begin{cases} 1, & \mathbf{x} \text{ in phase } i \\ 0, & \mathbf{x} \text{ otherwise} \end{cases}, \quad (5)$$

where $i = 1, \dots, q$ and q is the total number of phases [1]. In statistically homogeneous two-phase materials for which there are no preferred centers, the two-point probability function $S_2^{(i)}(\mathbf{r})$ measures the probability of finding two points \mathbf{x}_1 and \mathbf{x}_2 separated by displacement vector $\mathbf{r} = \mathbf{x}_2 - \mathbf{x}_1$ in phase i [1]. The three-point function $S_3^{(i)}(\mathbf{x}_1, \mathbf{x}_2, \mathbf{x}_3)$ gives the probability that triangle vertices \mathbf{x}_1 , \mathbf{x}_2 , and \mathbf{x}_3 all fall in phase i when placed randomly in the system [1]. For statistically homogeneous systems, $S_3^{(i)}$ depends only on the relative displacements of the sampling points, i.e., $S_3^{(i)}(\mathbf{x}_2 - \mathbf{x}_1, \mathbf{x}_3 - \mathbf{x}_1)$.

The autocovariance function is trivially related to the two-point function as

$$\chi_V(\mathbf{r}) \equiv S_2^{(i)}(\mathbf{r}) - \phi_i^2, \quad (6)$$

where ϕ_i is the volume fraction of phase i [1]. For d -dimensional isotropic materials, the autocovariance function depends only on the magnitude $r = |\mathbf{r}|$ of the displacement vector, and one can define the specific surface s in terms of the derivative of $\chi_V(r)$ at the origin [1,67], i.e.,

$$\left. \frac{d\chi_V(r)}{dr} \right|_{r=0} = -\frac{\omega_{d-1}}{\omega_d d} s, \quad (7)$$

where ω_d is the volume of a d -dimensional unit sphere

$$\omega_d = \frac{\pi^{d/2}}{\Gamma(1 + d/2)}. \quad (8)$$

We define the spectral density $\tilde{\chi}_V(\mathbf{k})$ as the Fourier transform of the autocovariance function at wavevector \mathbf{k} , i.e.,

$$\tilde{\chi}_V(\mathbf{k}) = \frac{1}{(2\pi)^d} \int_{\mathbb{R}^d} \chi_V(\mathbf{r}) e^{i\mathbf{k} \cdot \mathbf{r}} d\mathbf{k}. \quad (9)$$

The spectral density is a nonnegative real-valued function \mathbf{k} which is directly measurable in the laboratory from elastic scattering experiments [67]. In this work, we use Eq. (9) to compute the spectral density for model microstructures for which the autocovariance is known exactly.

We also consider several types of d -dimensional packings of N , radius a spheres in volume $V = L^d$ cubic simulation boxes under periodic boundary conditions. The spectral density for such materials is given by [1,38],

$$\tilde{\chi}_V(\mathbf{k}) = \frac{1}{V} \left| \sum_{j=1}^N \tilde{m}(|\mathbf{k}|; a) e^{-i\mathbf{k} \cdot \mathbf{r}_j} \right|^2. \quad (10)$$

Here, \mathbf{r}_j are the positions of each sphere center, a wavevector $\mathbf{k} = 2\pi(n_1, n_2, \dots, n_d)/L$ where $n_i \in \mathbb{Z}$ corresponds to the reciprocal lattice vectors of the unit cell, and $\tilde{m}(k; a) = (2\pi a/k)^{d/2} J_{d/2}(ka)$ is the Fourier transform of a sphere of radius a in which $J_\nu(x)$ is the Bessel function of order ν . We use spectral densities computed via Eq. (10) in integral (1) to demonstrate that using digitized representations of sphere packings (see Sections 3 and 4) has no significant effect on the accuracy of our spreadability simulations (see Section 6).

We rely on digitized representations of microstructures, which can represent systems with a variety of phase geometries and topologies, to compute the spectral densities for certain models considered in this work (see Section 6). Such digitized two-phase systems are materials consisting of square pixels (cubic voxels) in two (three) dimensions where each pixel (voxel) is occupied entirely by one phase, and a square

(cubic) domain has a side length of L pixels (voxels). One can show that the spectral density of such materials can be computed as

$$\tilde{\chi}_V(\mathbf{k}) = \frac{1}{L^d} \tilde{m}^2(\mathbf{k}) |\tilde{J}(\mathbf{k})|^2, \quad (11)$$

where $\tilde{m}(\mathbf{k})$ is the Fourier transform of a pixel (voxel) which is given by $\tilde{m}(\mathbf{k}) = \prod_{i=1}^d \text{sinc}(\pi n_i / L)$. The generalized collective coordinate [56,68] is defined as $\tilde{J}(\mathbf{k}) = \sum_{\mathbf{x}} \exp(i\mathbf{k} \cdot \mathbf{x}) (I^{(i)}(\mathbf{x}) - \phi_i)$ where \mathbf{x} corresponds to the positions of the pixel (voxel) centers.

2.2. Classification of hyperuniform and nonhyperuniform materials

The hyperuniformity of two-phase heterogeneous materials in d -dimensional space is defined by the following infinite-wavelength condition on the spectral density $\tilde{\chi}_V(\mathbf{k})$ [19,38]:

$$\lim_{|\mathbf{k}| \rightarrow 0} \tilde{\chi}_V(\mathbf{k}) = 0. \quad (12)$$

One can equivalently define hyperuniformity based on the local volume-fraction variance $\sigma_V^2(R)$ associated with a d -dimensional spherical observation window of radius R [19,38,69]. Henceforth, we explicitly consider two-phase materials but note that our methods may be generalized to n -phases. A two-phase material is hyperuniform if its variance grows in the large- R limit faster than R^d . This behavior contrasts that of typical disordered two-phase materials for which $\sigma_V^2(R)$ decays like the inverse of the spherical observation window volume. The hyperuniformity condition (12) implies that the autocovariance function $\chi_V(\mathbf{r})$ exhibits both positive and negative correlations such that its volume integral over all space is exactly zero [38,70]:

$$\int_{\mathbb{R}^d} \chi_V(\mathbf{r}) d\mathbf{r} = 0, \quad (13)$$

which is the direct-space sum rule for hyperuniformity.

The hyperuniformity concept provides a unified means to classify equilibrium and non-equilibrium states of matter, hyperuniform or not, according to their large-scale fluctuation characteristics. For statistically homogeneous hyperuniform two-phase materials [19,38] there are three different classes (scaling regimes) that describe the associated large- R behaviors of $\sigma_V^2(R)$ when the spectral density goes to zero as a power-law scaling (2) in the limit $|\mathbf{k}| \rightarrow 0$ [38]:

$$\sigma_V^2(R) \sim \begin{cases} R^{-(d+1)}, & \alpha > 1 \quad (\text{Class I}) \\ R^{-(d+1)} \ln R, & \alpha = 1 \quad (\text{Class II}) \\ R^{-(d+\alpha)}, & 0 < \alpha < 1 \quad (\text{Class III}). \end{cases} \quad (14)$$

Classes I and III are the strongest and weakest forms of hyperuniformity, respectively. Class I materials include all perfect crystals, many quasicrystals and exotic disordered materials [38]. Also belonging to class I are stealthy hyperuniform materials which are defined to be those which exhibit zero-scattering intensity for a set of wave vectors around the origin [70]:

$$\tilde{\chi}_V(\mathbf{k}) = 0 \quad \text{for } 0 \leq |\mathbf{k}| \leq K. \quad (15)$$

Examples of such stealthy materials are periodic packings of spheres, disordered sphere packings derived from stealthy point patterns, as well as specially designed stealthy hyperuniform dispersions [55,56,70].

Any statistically homogeneous nonhyperuniform two-phase material has a local variance with the following large- R scaling behaviors [71]:

$$\sigma_V^2(R) \sim \begin{cases} R^{-d}, & \alpha = 0 \quad (\text{typical nonhyperuniform}) \\ R^{-(d+\alpha)}, & -d < \alpha < 0 \quad (\text{antihyperuniform}). \end{cases} \quad (16)$$

A typical nonhyperuniform material has $\tilde{\chi}_V(0) > 0$ and thus $B = \tilde{\chi}_V(0)$ via Eq. (2) [38]. The spectral density of antihyperuniform systems is unbounded at the origin [71]:

$$\lim_{|\mathbf{k}| \rightarrow 0} \tilde{\chi}_V(\mathbf{k}) \rightarrow +\infty, \quad (17)$$

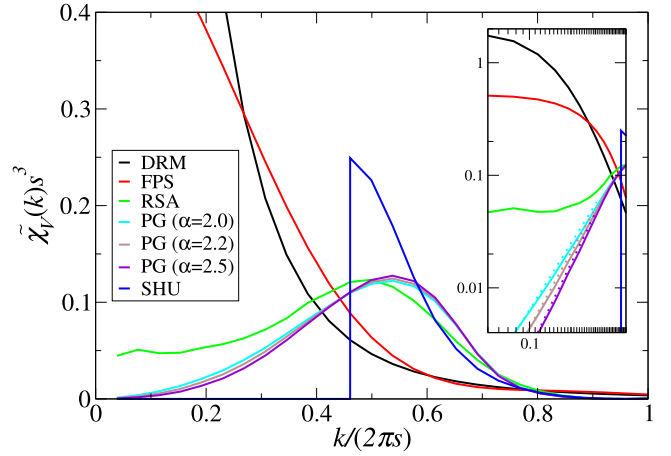


Fig. 2. Plots of the dimensionless spectral density $\tilde{\chi}_V(k)s^3$ vs. wavevector $k/(2\pi s)$ for the various (non)hyperuniform model two-phase systems we consider in this work. These models are listed from most nonhyperuniform (Debye random media) to most hyperuniform (stealthy disordered hyperuniform sphere packing). The inset shows the small- k behavior in a log-log plot to better illustrate how $\tilde{\chi}_V(k) \sim k^{-\alpha}$. The dashed lines correspond to plots of $k^{-\alpha}$ for the three different perfect glass systems.

thus making such systems diametrically opposed to hyperuniform ones. Examples of antihyperuniform systems include system at thermal critical points (e.g., liquid–vapor and magnetic critical points) [72,73], fractals [74], disordered nonfractals [75], and certain substitution tilings [76].

3. Model microstructures

We demonstrate the accuracy, versatility, and utility of our lattice diffusion algorithm by using it to compute the spreadability and entropy production rates for a variety of three dimensional disordered microstructures that represent a diverse class of nonhyperuniform and hyperuniform classes as described in Section 2.2. We note that this collection of systems constitutes a representative set of microstructures that span the disorder–order spectrum according to order metrics recently developed by Torquato et al. [69].

We consider all models with phase 2 volume fraction $\phi_2 = 0.25$ and specific surface $s = 0.1575$ such that their characteristic heterogeneity length scales are consistent with one another [69,77]. All results are averaged over 10 microstructural configurations. We also simulate the spreadability for phase-inverted versions of the models considered here in which each phase 1 voxel becomes phase 2 and vice versa. Such phase-inverted microstructures have the same exponent α as their progenitor system (see Eqs. (6) and (9)) and thus provide an additional way to measure α . The spectral densities for all three-dimensional systems considered here are plotted in Fig. 2.

3.1. Nonhyperuniform Debye random media

Debye random media (DRM) are models of nonhyperuniform two-phase media [67,78] which are defined entirely by the autocovariance function

$$\chi_V(r) = \phi_1 \phi_2 \exp(-r/a), \quad (18)$$

where $a > 0$ is a length-scale parameter. The specific surface s for Debye random media is equal to $\pi \phi_1 \phi_2 / a$ in 2D and $4 \phi_1 \phi_2 / a$ in 3D. Debye et al. [67] hypothesized the simple exponential form (18) to model 3D media with phases of “fully random shape, size, and distribution”, and were shown to be realizable in two [78–80] and three [81,82] dimensions. We consider this model because it is a good approximation of certain realistic heterogeneous materials [67], including Fontainebleau

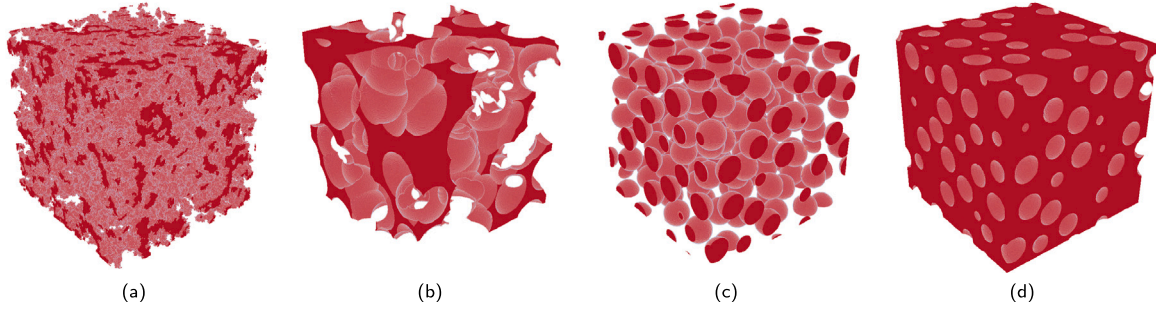


Fig. 3. Three-dimensional sample microstructures of (a) Debye random media, (b) fully penetrable spheres, (c) a stealthy hyperuniform sphere packing, and (d) the phase-inverted variant of the sphere packing in (c). For all structures, phase 1 is void space (transparent) and phase 2 is solid (red). (For interpretation of the references to color in this figure legend, the reader is referred to the web version of this article.)

sandstones [63], and its spreadability is known exactly in any space dimension [14]. In the infinite system limit, Debye random media possess arbitrarily large spherical pores in either phase [79,82,83]. Therefore, the finite-sized samples we consider here are challenging benchmark test cases for our algorithm.

We construct 401^3 cubic voxel realizations of Debye random media using an accelerated implementation [79,83] of the Yeong–Torquato construction algorithm [78,84]. In order to efficiently compare the results of our simulations to those produced by finite element methods, we examine two-dimensional samples of DRM with $\phi_2 = 0.5$ at a resolution of 501^2 square pixels. Such lower dimensional simulations are less computational resource intensive and thus more manageable for finite element simulations. These 2D realizations are constructed using the same protocol as the 3D ones. A rendering of a sample 3D DRM microstructure is shown in Fig. 3(a).

3.2. Nonhyperuniform media derived from thresholded Gaussian random fields

Gaussian random fields are constructed by a superposition of plane waves with randomly distributed wave vectors and phases such that the resulting field intensities are normally distributed [85]. Applying level cuts to, or thresholding, such scalar fields provides a computationally efficient means to generate various two-phase materials. This approach has seen prior use in generating model microstructures for various two-phase materials including carbonate rocks [86], Vycor glass [86], amorphous alloys [87], and aerogels [88]. We use the method of Lang and Potthoff [89] to generate Gaussian convolved scalar fields with nonhyperuniform field spectral density $\tilde{\psi}(k) = \exp[-k^2/(4\pi)]$. We subsequently threshold the resulting field to create a two-phase material with volume fraction $\phi_2 = 0.5$ and autocovariance function [1,87,90,91]

$$\chi_V(r) = \arcsin \left[e^{-\pi r^2} \right] / (2\pi) \quad (19)$$

and thus specific surface $s = 1/\sqrt{2\pi^3}$ [1,67]. The effective diffusion coefficient for such thresholded field microstructures at this composition is given exactly by [1,92]

$$D_e = \sqrt{D_1 D_2} \quad (\phi_2 = 1/2), \quad (20)$$

where D_1 and D_2 are the respective diffusion coefficients of phases 1 and 2. We simulate the spreadability for large, 5000^2 pixel thresholded fields for certain phase diffusion coefficient contrast ratios D_2/D_1 within the interval [1,25]. We ascertain D_e from these data (see Section 6.2 for details) and compare these values to the exact result (20).

3.3. Nonhyperuniform fully penetrable spheres

We also consider the well-known model of “fully penetrable spheres” (FPS) [1,93]. These nonhyperuniform systems are prepared by decorating all points of a Poisson point process with d -dimensional spheres of radius a that are free to overlap with one another. The simplicity of the n -body statistics of these model material microstructures enables us to exactly express the $\chi_V(r)$ of the matrix phase which we designate as phase 2 in this work [1,93]:

$$\chi_V(r) = \exp \left[-\eta \frac{v_2(r; a)}{v_1(a)} \right] - \phi_2^2, \quad (21)$$

where $\eta = -\ln(\phi_2)$ and $v_2(r; a)$ is the union volume of two spheres of radius a , the expression for which can be found in Ref. [1]. The specific surface for d -dimensional FPS is given by [94] $s = -d\phi_2 \ln(\phi_2)$. We consider FPS systems with $N = 2500$ spheres. For simulations, the FPS systems as well as all subsequent systems are digitized to a resolution of 1001^3 cubic voxels. A rendering of a sample FPS microstructure is shown in Fig. 3(b).

3.4. Nonhyperuniform random sequentially adsorbed spheres

Random sequential adsorption (RSA) is a time-dependent process that irreversibly, randomly, and sequentially places nonoverlapping spheres into space [1,95]. In the infinite-time limit, the system becomes saturated, i.e., no additional sphere can be inserted into the system. While not hyperuniform [96], the non-overlapping constraint introduces a significant amount of order into these systems over that found in the other nonhyperuniform models considered here. Since the RSA packings we consider here are well below the saturation-limiting packing fraction of about 0.3841... [96], they possess arbitrarily large spherical pores in phase 1 in the infinite-system limit. We generate $N = 2500$ sphere RSA packings using the voxel-list algorithm developed by Zhang and Torquato [96]. The specific surface for all d -dimensional monodisperse sphere packings with radius a is $s = d\phi_2$ [94].

3.5. Hyperuniform sphere packings derived from “perfect glasses”

Perfect glasses (PG’s) [97] are hyperuniform many-body systems with positive bulk and shear moduli that banish any crystalline or quasicrystalline phases and are unique disordered states up to trivial symmetries [98]. Sphere packings derived from perfect glasses provide a rare opportunity to create two-phase microstructures with precisely controllable spectral density exponent α . Note that the size of pores in

phase 1 of sphere packings derived from perfect glass point patterns is bounded in the infinite-system limit [99]. We generate $N = 2500$ perfect glass point configurations using the collective-coordinates optimization scheme [68] according to the specifications provided in Ref. [97].

3.6. Disordered stealthy hyperuniform sphere packings

Like crystals, disordered stealthy hyperuniform (SHU) materials, exhibit zero-scattering intensity for a set of wave vectors around the origin (see. Eq. (15)). By virtue of being disordered, however, this zero-scattering region is directionally-independent. Such a combination of hidden order at large length scales and isotropy often endows stealthy hyperuniform materials with exotic physical properties like isotropic photonic and phononic band gaps [39–41,43,100], as well as optimal transport properties [55,70]. We generate $N = 2500$ disordered stealthy hyperuniform radius a sphere packings with $Ka = 2.15$, by decorating stealthy hyperuniform point patterns prepared with the collective coordinate procedure [45,55]. Note that the size of pores in phase 1 of sphere packings derived from stealthy hyperuniform point patterns is bounded in the infinite-system limit [101,102]. Renderings of a sample SHU sphere packing and its phase-inverted variant are shown in Figs. 3(c) and 3(d), respectively.

4. Lattice diffusion algorithm

Algorithmic details of our lattice diffusion algorithm are summarized here. Our algorithm uses digitized representations of two-phase material microstructures. Beyond the various practical benefits of using such representations discussed in Sections 1 and 2.1, such digitized models have a natural array representation on the computer that facilitates the computation of vector derivative quantities without requiring complicated meshing routines. Importantly, we show that using digitized representations does not reduce the accuracy of our simulated spreadability and entropy production results as demonstrated in Section 6.

For concreteness, we consider a hypercubic digitized representation of the microstructure, i.e., square (cubic) pixels in two (three) dimensions to which the random walkers are bound. At time $t = 0$, all walkers are distributed uniformly throughout phase 2. For our simulations, we found that 10^6 walkers per lattice site ensures sufficient sampling of the microstructure. The walkers move along the lattice according to the algorithm developed by McCarthy [103,104]. Here, phase 1 and 2 lattice sites have diffusion coefficients D_1 and D_2 and we assume without loss of generality that $D_2/D_1 \geq 1$. After each time step Δt , the N_w walkers at each lattice site i with diffusion coefficient D_i will randomly select, with equal probability, one of the $2d$ neighboring sites j, k, l, \dots with respective diffusion coefficients D_j, D_k, D_l, \dots . Each walker will then hop to its selected neighbor x with probability,

$$P_{i,x} = \frac{2D_i D_x}{D_i + D_x} \quad (22)$$

or remain on site i with probability $1 - P_{i,x}$ [103,104]. Note that in this scheme, the diffusion coefficients must be scaled such that $D_2 = 1$ to ensure that hopping probability (22) is normalized. Also note that when $D_1 = D_2$, $P_{i,x} = 1$ and thus each walker hops randomly to one of its nearest neighbors at every time step; corresponding to an unbiased random walk. The simulations are made computationally efficient by distributing the work for each system evolution step among multiple processors. Here, we specifically assign each GPU thread to a cluster of lattice sites. With this scheme, it takes around 5.5 h to run a 5×10^4 step simulation on an 80 Gigabyte NVIDIA® A100 GPU.

Plots of the excess spreadability for two-dimensional Debye random media computed via the lattice diffusion algorithm, commercial finite element software COMSOL Multiphysics®, as well as the exact analytical expression derived by Torquato [14] are shown in Fig. 4. We

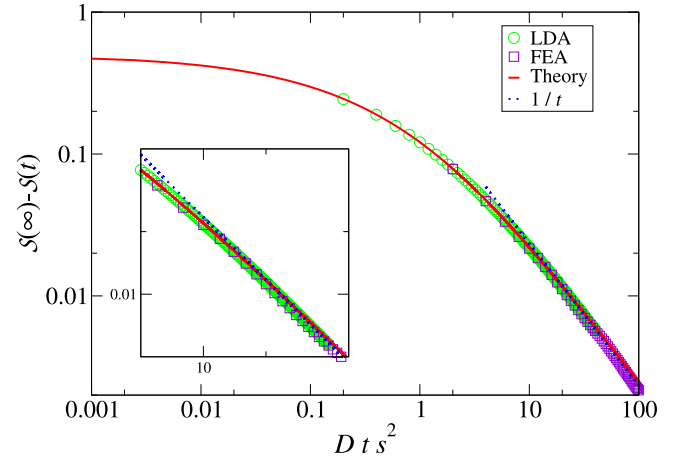


Fig. 4. Log-log plots of dimensionless time Dts^2 vs. the excess spreadability $S(\infty) - S(t)$ computed via the lattice diffusion algorithm (circles) and commercial finite element analysis (FEA) software (squares) for 2D Debye random media with $\phi_2 = 0.5$. The simulated results are compared to the exact analytical result derived by Torquato [14] (solid line). The inset shows the long-time asymptotic scaling of the excess spreadability, clearly indicating that $S(\infty) - S(t) \sim 1/t$ (dotted line) as predicted by the power-law (3). The simulated results have negligibly small error bars that cannot be distinguished on the scale of this figure.

see that the LDA computes excess spreadabilities which are completely consistent with those computed via exact theories and commercial finite element techniques across all time-scales. It is crucial to note that we can correctly extrapolate that $\alpha = 0$ for Debye random media from the long-time regime of $S(\infty) - S(t)$ computed with our algorithm.

5. Entropy production rate

The entropy production rate per unit volume $\dot{s}(t)$ of the diffusion process associated with the spreadability is a measure of the rate of energy dissipation. For an irreversible time-dependent diffusion process in an infinite medium in \mathbb{R}^d , $\dot{s}(t)$ is defined as [1]

$$\dot{s}(t) = \frac{1}{V} \int_{\mathbb{R}^d} |\nabla c(\mathbf{x}, t)|^2 d\mathbf{x}, \quad (23)$$

where the concentration field is given in terms of the d -dimensional Green's function solution for the time-dependent diffusion equation. Using the method of Prager [15] and Torquato [14], we derive the following expression for $\dot{s}(t)$ for statistically isotropic and homogeneous media in dimension $d \geq 2$:

$$\dot{s}(t) = q_d(t) \int_0^\infty r_1^d dr_1 \int_0^\infty r_2^d dr_2 \int_0^\pi \cos(\theta) d\theta \times S_2(r_3) G(r_1, t) G(r_2, t). \quad (24)$$

Here, $q_d(t) \equiv \Omega(d)\Omega(d-1)c_0^2/[(4\pi Dt)^d(2Dt)^2]$ where $\Omega(d) = d\pi^{d/2}/\Gamma(1+d/2)$ is the surface area of a d -dimensional unit sphere, $r_3 = \sqrt{r_1^2 + r_2^2 - 2r_1r_2\cos(\theta)}$ where θ is the angle between vectors \mathbf{r}_1 and \mathbf{r}_2 , and $G(r, t) \equiv \exp[-r^2/(4Dt)]$. The details of the derivation of (24) are provided in the Supplementary Material (SM).

We also consider the entropy production rate in phase i , which is defined as

$$\dot{s}^{(i)}(t) = \frac{1}{V} \int_{\mathbb{R}^d} |\nabla c(\mathbf{x}, t)|^2 I^{(i)}(\mathbf{x}) d\mathbf{x}. \quad (25)$$

We find that the entropy production in phase 2 is given by the integral

$$\dot{s}^{(2)}(t) = q_d(t) \int_0^\infty r_1^d dr_1 \int_0^\infty r_2^d dr_2 \int_0^\pi \cos(\theta) d\theta \times S_3(r_1, r_2, r_3) G(r_1, t) G(r_2, t), \quad (26)$$

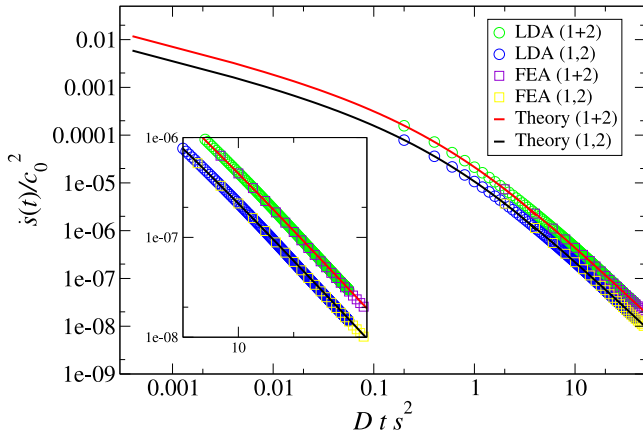


Fig. 5. Log-log plots of dimensionless time Dts^2 vs. the dimensionless entropy production rate $\dot{s}(t)/c_0^2$ for the individual phases (1, 2) as well as the entire material (1+2) computed via the LDA (circles) and commercial FEA software (squares) for 2D Debye random media with $\phi_2 = 0.5$. The simulated entropy production rates are compared to those computed via integrals (24) and (26) (solid lines). The inset highlights the long-time power-law decay of the entropy production rate. The simulated results have negligibly small error bars that cannot be distinguished on the scale of this figure.

and that $\dot{s}^{(1)}(t)$ can be determined via the additivity rule $\dot{s}(t) = \dot{s}^{(1)}(t) + \dot{s}^{(2)}(t)$. In general, integrals (24) and (26) must be evaluated numerically.

The $t = 0$ initial condition for the spreadability has all solute distributed uniformly in phase 2 with concentration c_0 , i.e.,

$$c(\mathbf{x}, 0) = c_0 \mathcal{I}^{(2)}(\mathbf{x}). \quad (27)$$

Since the phase indicator function (5) contains jump discontinuities at the phase boundaries, the gradient of the initial concentration consists of Dirac delta functions along the phase boundaries [1]. It immediately follows from definition (27) that $\dot{s}(t)$ and $\dot{s}^{(i)}(t)$ diverge to infinity as $t \rightarrow 0^+$. As the spreadability approaches its equilibrium steady-state as $t \rightarrow \infty$, $\dot{s}(t)$ and $\dot{s}^{(i)}(t)$ will go to 0.

Plots of the entropy production rate for two-dimensional Debye random media computed via the lattice diffusion algorithm, commercial finite element software, as well as the integrals (24) and (26) are shown in Fig. 5. Here, we use Debye microstructures with $\phi_2 = 0.5$ because the three-point correlation function $S_3^{(i)}$ for these microstructures is known exactly (see the SM for details). We see that the LDA computes $\dot{s}(t)$ which are completely consistent with those computed via exact theories and commercial finite element techniques across all time-scales. Note that in the long-time asymptotic regime, the entropy production rates for Debye random media exhibit a power-law decay. Also note how $\dot{s}^{(1)}(t) = \dot{s}^{(2)}(t)$ here.

6. Simulation results

6.1. The spreadability and entropy production rate

In this section, we present numerical results for the simulated spreadabilities and entropy production rates for the various model systems considered in this work. We extrapolate the exponent α for non-stealthy materials using a variation of the fitting technique introduced in Ref. [62], and measure the accuracy of these values through the difference $\Delta\alpha = \alpha^{\text{extrapolated}} - \alpha^{\text{true}}$. To quantify the overall accuracy of our simulated excess spreadabilities, we use the error estimate $\Delta S = (1/N_t) \sum_i |\delta[S(\infty) - S(t)]|$ [79,83] where N_t is the number of discrete simulation time-steps and $\delta[S(\infty) - S(t)]$ is the difference between the simulated and integrated excess spreadabilities at time t .

For Debye random media and fully penetrable spheres, the integrated excess spreadability was computed via integral (1) using their

Table 1

Tabulated measurements of the accuracy of diffusion spreadability data computed via our simulation algorithm. In the Model column, note that (i) denotes the phase-inverted variation of a given microstructure. The central column ($\Delta\alpha$) lists numerical deviations of simulation extrapolated α from the true value, and the right column (ΔS) lists averaged numerical deviations of the simulated excess spreadability from the integrated one. Overall, the small values of $\Delta\alpha$ and ΔS underscore the accuracy of our simulation algorithm.

Model	$\Delta\alpha$	$\Delta[S(\infty) - S(t)]$
DRM	5.52×10^{-3}	3.94×10^{-4}
DRM (i)	5.79×10^{-3}	1.32×10^{-4}
FPS	8.80×10^{-3}	1.16×10^{-3}
FPS (i)	2.19×10^{-3}	6.10×10^{-4}
RSA	-6.39×10^{-2}	3.06×10^{-4}
RSA (i)	-6.36×10^{-2}	1.89×10^{-4}
PG, $\alpha = 2.0$	2.51×10^{-3}	7.95×10^{-4}
PG, $\alpha = 2.0$ (i)	2.51×10^{-3}	1.48×10^{-4}
PG, $\alpha = 2.2$	7.37×10^{-3}	8.05×10^{-4}
PG, $\alpha = 2.2$ (i)	7.37×10^{-3}	1.46×10^{-4}
PG, $\alpha = 2.5$	-7.96×10^{-3}	8.08×10^{-4}
PG, $\alpha = 2.5$ (i)	-7.99×10^{-3}	1.43×10^{-4}
SHU	—	7.14×10^{-4}
SHU (i)	—	1.59×10^{-4}

respective autocovariance functions (18) and (21). Integrated $S(\infty) - S(t)$ for the sphere packings used spectral densities computed via Eq. (10), while those for the phase-inverted microstructures used spectral densities computed through Eq. (11). Values of $\Delta\alpha$ and ΔS for all model microstructures are listed in Table 1. The small deviations in the extrapolated exponent ($10^{-3} \lesssim \Delta\alpha \lesssim 10^{-2}$) as well as the small error in the simulated spreadability ($10^{-4} \lesssim \Delta S \lesssim 10^{-3}$) indicate the accuracy of our algorithm and its overall robustness to digitization effects. Plots of the simulated excess spreadabilities for selected microstructures are shown in Fig. 6(a).

The simulated entropy production rates $\dot{s}(t)$ and $\dot{s}^{(2)}(t)$ for the model microstructures are shown in Fig. 6(b). It is seen that non-stealthy media have entropy production rates that exhibit power-law decays in the long-time asymptotic regime. Notably, $\dot{s}(t)$ decays more rapidly as the exponent α increases, with stealthy materials having apparently exponentially fast decays. Overall, these trends in the entropy production results indicate that hyperuniform materials have smaller rates of energy dissipation than any nonhyperuniform materials. In Fig. 6(b), note how fully penetrable spheres exhibit the lowest entropy production rates for small times ($10^{-4} < Dts^2 < 10^{-2}$). This behavior can be attributed to the high-degree of clustering in these systems at short length-scales [69].

Also note how our simulation results demonstrate that the rank orderings of different microstructures based on their long-time asymptotic spreadabilities and entropy production rates are consistent with one another. Despite the entropy production rates for phases 1 and 2 incorporating one-, two-, and three-point statistics, they still predict the same ordering of microstructures as $\dot{s}(t)$ and $S(\infty) - S(t)$ in the long-time asymptotic regime—both of which incorporate just one- and two-point statistics. This behavior is due to the fact that the three-point correlation function $S_3^{(i)}(r_1, r_2, r_3)$ for disordered systems differs from two-point information only for relatively small triangles (with side length of the order of the correlation length), which does not determine the large-length or long-time scale behavior [1]. In other words, in the long-time asymptotic regime of $\dot{s}^{(2)}(t)$, the factor of $S_3^{(i)}(r_1, r_2, r_3)$ in integral (26) effectively contributes only one- and two-point level correlations.

6.2. The spreadability with different phase diffusion coefficients

In this section, we present numerical results for the simulated spreadability for multiple values of the phase diffusion coefficient

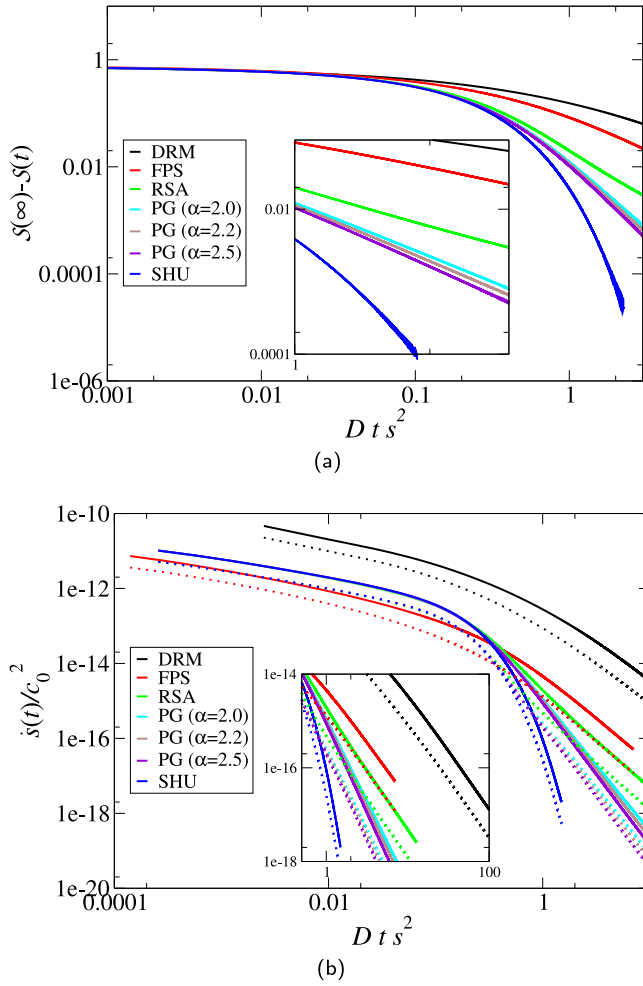


Fig. 6. Log-log plots of dimensionless time Dts^2 vs. (a) excess spreadability $S(\infty) - S(t)$ and (b) dimensionless specific entropy production rate $\dot{s}(t)/c_0^2$ computed via the lattice diffusion algorithm. In (b), the solid and dotted lines correspond to the entropy production rates for the entire system ($\dot{s}(t)$) and phase 2 ($\dot{s}^{(2)}(t)$), respectively. The inset plots in (a) and (b) highlight the long-time behavior of the curves. Note how the rank orderings of the microstructures based on their long-time asymptotic spreadabilities and entropy production rates are consistent with one another. The same ranking is predicted by $\dot{s}^{(1)}(t)$, but those curves have been omitted in order to keep the plot readable.

contrast ratio D_2/D_1 that lie within the interval $[1, 25]$. We use the nonhyperuniform two-dimensional thresholded Gaussian random field microstructure described in Section 3.2 as our model system. These excess spreadabilities are plotted in Fig. 7(a). When scaling the horizontal axis by $D_e s^2$, where D_e is given by Eq. (20), note how all spreadability curves collapse together in the short- and long-time regimes. This collapse in the long-time regime is consistent with Torquato's mapping between the NMR PFGSE amplitude and the excess spreadability in which D is replaced by D_e in Eq. (3).

In the intermediate-time regime ($10^2 < D_e t s^2 < 10^4$), the curves deviate from the $D_2/D_1 = 1$ case progressively more as D_2/D_1 increases; with $S(\infty) - S(t)$ for $D_2/D_1 = 25$ being $\sim 5\times$ greater than $S(\infty) - S(t)$ for $D_2/D_1 = 1$ at $Dts^2 = 200$. This deviation is due to the tendency of the walkers to remain localized in phase 2 for longer due to its higher diffusion coefficient; thus making $S(\infty) - S(t)$ take longer to reach its long-time asymptotic scaling regime.

These simulations of the spreadability when $D_2/D_1 \neq 1$ can be used to estimate the effective diffusion coefficient of the material. Specifically, we can fit the integrated spreadability (1) using autocovariance (19) to our simulated data in the long-time regime via residual sum of squares methods using the diffusion coefficient as a free parameter.

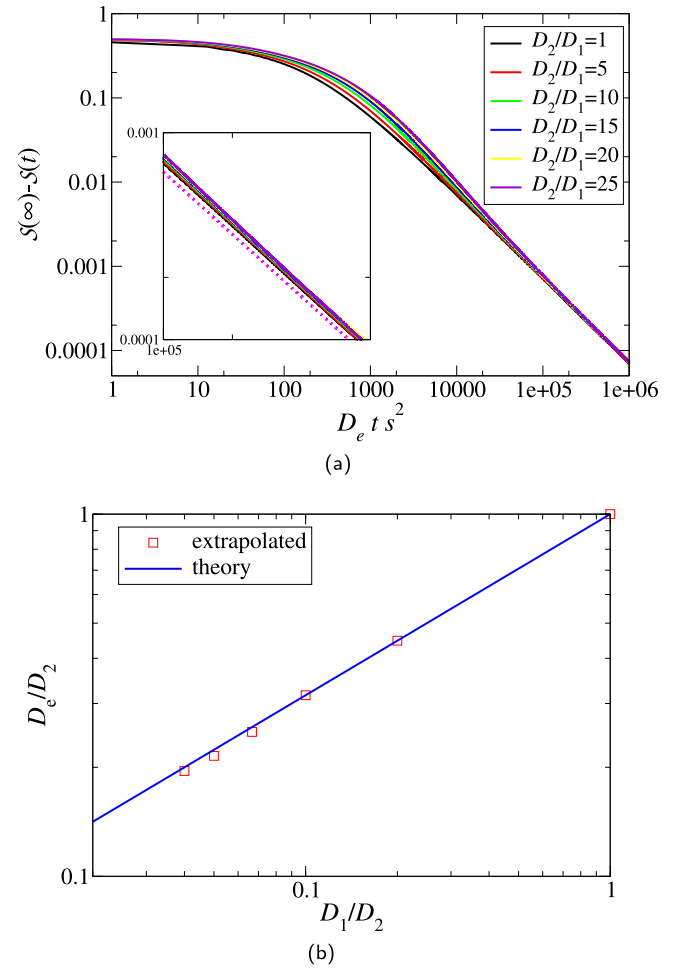


Fig. 7. (a) Log-log plots of the simulated excess spreadability $S(\infty) - S(t)$ vs. dimensionless time $D_e t s^2$ with various contrast ratios D_2/D_1 for the 2D nonhyperuniform thresholded Gaussian random field microstructure. Note how the curves collapse together in the short- and long-time regimes. The dotted line plotted in the inset highlights the $1/t$ scaling exhibited by all curves in the long-time regime. (b) Log-log plot of the dimensionless effective diffusion coefficient D_e/D_2 as a function of reciprocal contrast ratio D_1/D_2 . The scatter plots correspond to values extrapolated from simulated spreadability data in (a) while the solid line corresponds to the theoretical result (20). Due to the requirement that the diffusion coefficients must be rescaled such that $D_2 = 1$ and $D_1 < D_2$ for the simulations, we plot the reciprocal contrast ratio D_1/D_2 on the horizontal axis in (b).

Values of effective diffusion coefficients extrapolated via this method are compared to the exact analytical result (20) for various contrast ratios in Fig. 7(b). We see that the extrapolated values of D_e agree reasonably well with the theoretical ones, with the largest deviation being of order 10^{-2} for larger contrast ratios $D_2/D_1 \geq 20$. Greater accuracy in the extrapolated values of D_e for larger contrast ratios is expected to be achieved by using larger sample microstructures.

7. Conclusions

In summary, we have developed a computationally efficient and powerful simulation method for directly computing the diffusion spreadability and the entropy production rate of the associated diffusion process using random walk methods. We have tested our algorithm by applying it to a variety of digitized two- and three-dimensional (non)hyperuniform model material microstructures which span the order/disorder spectrum. Our benchmark tests also demonstrate that our algorithm captures diffusion spreadability phenomena as accurately as commercial finite element software does, while being free to use

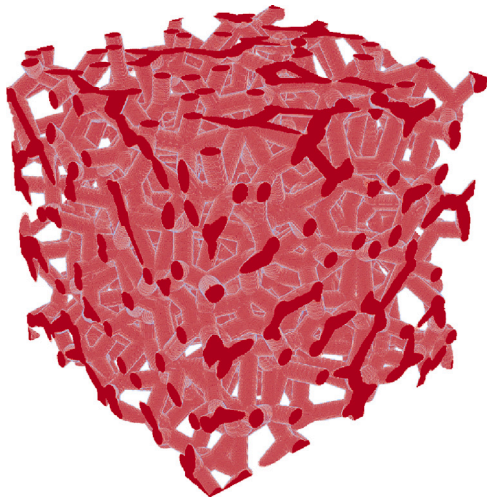


Fig. 8. A self-supporting stealthy hyperuniform network material derived from a stealthy sphere packing. Like its progenitor sphere packing, this material also has phase 2 volume fraction $\phi_2 = 0.25$.

and leveraging graphics processing units for extremely high performance. Moreover, the agreement between our simulated spreadabilities and those computed via scattering information, i.e., through Eq. (1), demonstrate that our method can serve as an additional and independent analysis of a material's microstructure via diffusion measurements, as in the case of NMR [58] and MRI methods [60]. Importantly, we have found that the digitization requirement of our method does not appreciably alter the accuracy of its results.

Since our algorithm enables us to determine the concentration field $c(\mathbf{x}, t)$, we were able to compute, for the first time, the entropy production rate associated with the spreadability's diffusion process. From our corresponding analytical work, we found that the entropy production rate for phases 1 and 2 (26) is sensitive to one-, two-, and three-point microstructural statistics. Our simulation results demonstrate that the rank orderings of different disordered model microstructures based on their long-time asymptotic spreadabilities and entropy production rates are consistent with one another, even though the latter incorporates additional third-order statistics, for reasons noted in Section 6.1. However, such consistencies between the rankings based on the spreadabilities and entropy production rates may not apply in the case of ordered (periodic) media, since the three-point correlation functions of ordered materials contain an appreciable amount of microstructural information above what is included in their two-point functions [105]. Therefore, in the future, it would be interesting to examine whether the rank orderings for the long-time asymptotic spreadabilities and entropy production rates are still consistent with one another for ordered materials.

In material design problems, it is desirable to consider microstructures that may be realized using modern 3D printing techniques [106]. For example, as discussed in Ref. [107], the inverted sphere packing microstructures considered here can be 3D printed since the solid phase is self supporting by virtue of its topological connectedness. We note that one can also make self-supporting (and thus 3D-printable) network materials from the sphere packings by treating the edges of their respective Voronoi tessellations as cylindrical struts [108,109]. An attractive benefit of such network structures is their generally low volume fraction and thus low weight. A rendering of such a network structure derived from a stealthy hyperuniform sphere packing is shown in Fig. 8.

We also used our algorithm to conduct the first analysis of the more physically reasonable case of the spreadability when the phase diffusion coefficients are different. The LDA simulations show that the long-time asymptotic scaling of the spreadability in this scenario is accurately

captured by the mapping between the spreadability and the NMR PFGSE amplitude identified by Torquato [14] in which the effective diffusion coefficient D_e is substituted for D in Eq. (3). Given these findings, and the previously shown connections of $S(r)$ to NMR PFGSE and diffusion MRI techniques [14], our work has implications for such experimental methodologies as well. Specifically, as the spreadability for cases when $D_2/D_1 \neq 1$ is also a sensitive probe of short-, intermediate-, and large-scale structural features, future experiments could be designed to realize the spreadability in the laboratory; a potentially useful characterization technique when scattering information is unobtainable.

Interestingly, there is a clear deviation of this effective theory and the simulated results in the intermediate-time regime that grows with the contrast ratio D_2/D_1 . This deviation is caused by the tendency of the walkers to preferentially localize in the phase with the higher diffusion coefficient. As noted in Ref. [14], the development of an exact theoretical description of the spreadability when $D_2/D_1 \neq 1$ is an outstanding problem for future work. Torquato suggested that such a problem could be approached by using the “strong-contrast” methodology which has been used to derive exact expressions for the effective physical properties of two-phase media in terms of an infinite set of correlation functions and phase contrast ratios [1]. Naturally, our LDA simulations can be used as a numerical benchmark in the development of such a theory.

In summary, our results highlight how the simulated diffusion spreadability provides critical information about material microstructures and corresponding effective physical properties. Moreover, our work further demonstrates the power of dynamical, physical-property based probes for applications in materials design and discovery. For example, our algorithm can be used to accurately extract the exponent α of a microstructure, thus providing a novel route to determine the (non)hyperuniformity of complex microstructures [42,47,60,79,83,86,87,91,110,111] independently of noisy [61,62] spectral density data. Our algorithm could also be applied to the inverse problem of designing a material with desirable time-dependent diffusion properties. One could devise a realizable $\tilde{\chi}_V(\mathbf{k})$ or $\chi_V(\mathbf{r})$ whose short-, intermediate-, and long-range correlations capture the desired short-, intermediate-, and long-time diffusion regimes of the spreadability. The degree of order/disorder on various length scales can be tailored using recently proposed order metrics for two-phase media [69]. Microstructures with such designed $\tilde{\chi}_V(\mathbf{k})$ and $\chi_V(\mathbf{r})$ could be generated using inverse methods described in Refs. [56,78]. Finally, our simulation algorithm can provide an assessment of how well the designed microstructures realize their prescribed two-point statistics across length scales independently of scattering data, while simultaneously providing information about their effective diffusion and associated energy dissipation properties.

Declaration of competing interest

The authors declare that they have no known competing financial interests or personal relationships that could have appeared to influence the work reported in this paper.

Acknowledgments

This work was sponsored by the Army Research Office, United States and was accomplished under Cooperative Agreement Number W911NF-22-2-0103, as well as the Air Force Office of Scientific Research Program, United States under award No. FA9550-18-1-0514. The authors thank the Princeton Institute for Computational Science and Engineering (PICSciE) for the computational resources. M.S. is very grateful to Charles Maher and Haina Wang for helpful discussions, and to Jaekuk Kim for his assistance with creating the stealthy hyperuniform sphere packings. S.T. thanks the Institute for Advanced Study for their hospitality during his sabbatical leave there.

Appendix A. Supplementary data

Supplementary material related to this article can be found online at <https://doi.org/10.1016/j.actamat.2023.118857>.

References

- [1] S. Torquato, Random Heterogeneous Materials: Microstructure and Macroscopic Properties, Springer-Verlag, New York, 2002.
- [2] M. Sahimi, Heterogeneous Materials I: Linear Transport and Optical Properties, Springer-Verlag, New York, 2003.
- [3] P. Tahmasebi, Accurate modeling and evaluation of microstructures in complex materials, *Phys. Rev. E* 97 (2018) 023307.
- [4] V.J. Wedeen, P. Hagmann, W.-Y.I. Tseng, T.G. Reese, R.M. Weisskoff, Mapping complex tissue architecture with diffusion spectrum magnetic resonance imaging, *Magn. Reson. Med.* 54 (2005) 1377–1386.
- [5] Probing local diffusion and reaction in a porous catalyst pellet, *J. Catalysis* 381 (2020) 285–294.
- [6] K.R. Brownstein, C.E. Tarr, Importance of classical diffusion in NMR studies of water in biological cells, *Phys. Rev. A* 19 (1979) 2446–2453.
- [7] R.S. Langer, N.A. Peppas, Present and future applications of biomaterials in controlled drug delivery systems, *Biomaterials* 2 (1981) 201–214.
- [8] G.W. Milton, The Theory of Composites, Cambridge University Press, Cambridge, England, 2002.
- [9] B. Patel, T.I. Zohdi, Numerical estimation of effective electromagnetic properties for design of particulate composites, *Mater. Des.* 94 (2016) 546–553.
- [10] S. Torquato, Morphology and effective properties of disordered heterogeneous media, *Int. J. Solids Struct.* 35 (1998) 2385.
- [11] A. Chremos, J.F. Douglas, Particle localization and hyperuniformity of polymer-grafted nanoparticle materials, *Ann. Phys.* 529 (5) (2017) 1600342.
- [12] A. Chremos, J.F. Douglas, Hidden hyperuniformity in soft polymeric materials, *Phys. Rev. Lett.* 121 (2018) 258002.
- [13] M. Huang, W. Hu, S. Yang, Q.-X. Liu, H. Zhang, Circular swimming motility and disordered hyperuniform state in an algae system, *Proc. Natl. Acad. Sci.* 118 (18) e2100493118.
- [14] S. Torquato, Diffusion spreadability as a probe of the microstructure of complex media across length scales, *Phys. Rev. E* 104 (2021) 054102.
- [15] S. Prager, Interphase transfer in stationary two-phase media, *Chem. Eng. Sci.* 18 (1963) 227–231.
- [16] A.K. Sen, S. Torquato, Effective conductivity of anisotropic two-phase composite media, *Phys. Rev. B* 39 (1989) 4504–4515.
- [17] S. Torquato, J. Kim, Nonlocal effective electromagnetic wave characteristics of composite media: Beyond the quasistatic regime, *Phys. Rev. X* 11 (2021) 021002.
- [18] S. Torquato, F.H. Stillinger, Local density fluctuations, hyperuniform systems, and order metrics, *Phys. Rev. E* 68 (2003) 041113.
- [19] C.E. Zachary, S. Torquato, Hyperuniformity in point patterns and two-phase heterogeneous media, *J. Stat. Mech. Theory Exp.* 2009 (2009) P12015.
- [20] M. Florescu, S. Torquato, P.J. Steinhardt, Complete band gaps in two-dimensional photonic quasicrystals, *Phys. Rev. B* 80 (2009) 155112.
- [21] Y. Jiao, T. Lau, H. Hatzikirou, M. Meyer-Hermann, J.C. Corbo, S. Torquato, Avian photoreceptor patterns represent a disordered hyperuniform solution to a multiscale packing problem, *Phys. Rev. E* 89 (2014) 022721.
- [22] C. De Rosa, F. Auricemma, C. Diletto, R. Di Girolamo, A. Malafrente, P. Morvillo, G. Zito, G. Rusciano, G. Pesce, A. Sasso, Toward hyperuniform disordered plasmonic nanostructures for reproducible surface-enhanced Raman spectroscopy, *Phys. Chem. Chem. Phys.* 17 (2015) 8061–8069.
- [23] O. Leseur, R. Pierrat, R. Carminati, High-density hyperuniform materials can be transparent, *Optica* 3 (2016) 763–767.
- [24] T. Ma, H. Guerboukha, M. Girard, A.D. Squires, R.A. Lewis, M. Skorobogatiy, 3D printed hollow-core terahertz optical waveguides with hyperuniform disordered dielectric reflectors, *Adv. Opt. Mater.* 4 (2016) 2085–2094.
- [25] L.S. Froufe-Pérez, M. Engel, J. José Sáenz, F. Scheffold, Transport phase diagram and Anderson localization in hyperuniform disordered photonic materials, *Proc. Natl. Acad. Sci.* 114 (2017) 9570–9574.
- [26] H. Zhang, H. Chu, H. Giddens, W. Wu, Y. Hao, Experimental demonstration of lüneburg lens based on hyperuniform disordered media, *Appl. Phys. Lett.* 114 (2019) 053507.
- [27] F. Sgrignuoli, L. Dal Negro, Hyperuniformity and wave localization in pinwheel scattering arrays, *Phys. Rev. B* 103 (2021) 224202.
- [28] F. Sgrignuoli, S. Torquato, L. Dal Negro, Subdiffusive wave transport and weak localization transition in three-dimensional stealthy hyperuniform disordered systems, *Phys. Rev. B* 105 (2022) 064204.
- [29] A. Rohfritsch, J.-M. Conoir, T. Valier-Brasier, R. Marchiano, Impact of particle size and multiple scattering on the propagation of waves in stealthy-hyperuniform media, *Phys. Rev. E* 102 (2020) 053001.
- [30] H. Zhang, Q. Cheng, H. Chu, O. Christogeorgos, W. Wu, Y. Hao, Hyperuniform disordered distribution metasurface for scattering reduction, *Appl. Phys. Lett.* 118 (2021) 101601.
- [31] Y. Zheng, D. Chen, L. Liu, Y. Liu, M. Chen, H. Zhuang, Y. Jiao, Topological transformations in hyperuniform pentagonal two-dimensional materials induced by stone-wales defects, *Phys. Rev. B* 103 (2021) 245413.
- [32] D. Chen, Y. Zheng, C.-H. Lee, S. Kang, W. Zhu, H. Zhuang, P. Huang, Y. Jiao, Nearly hyperuniform, nonhyperuniform, and antihyperuniform density fluctuations in two-dimensional transition metal dichalcogenides with defects, *Phys. Rev. B* 103 (2021) 224102.
- [33] D. Chen, Y. Zheng, L. Liu, G. Zhang, M. Chen, Y. Jiao, H. Zhuang, Stone-wales defects preserve hyperuniformity in amorphous two-dimensional networks, *Proc. Natl. Acad. Sci.* 118 (2021) e2016862118.
- [34] Multihyperuniform long-range order in medium-entropy alloys, *Acta Mater.* 246 (2023) 118678.
- [35] N. Granchi, R. Spalding, M. Lodde, M. Petruzzella, F. Otten, A. Fiore, F. Intonti, R. Sapienza, M. Florescu, M. Gurioli, Near-field investigation of luminescent hyperuniform disordered materials, *Adv. Opt. Mater.* 10 (8) 2102565.
- [36] S. Aebly, G. Aubry, L. Froufe-Pérez, F. Scheffold, Fabrication of hyperuniform dielectric networks via heat-induced shrinkage reveals a bandgap at telecom wavelengths, *Adv. Opt. Mater.* 10 (14) 2200232.
- [37] P. Piechulla, R. Wehrspohn, A. Sprafke, Toward hyperuniform disorder via self-assembly of bidisperse colloidal patterns at an electrode, *Adv. Mater. Interfaces* 2201395.
- [38] S. Torquato, Hyperuniform states of matter, *Phys. Rep.* 745 (2018) 1–95.
- [39] M. Florescu, S. Torquato, P.J. Steinhardt, Designer disordered materials with large complete photonic band gaps, *Proc. Natl. Acad. Sci.* 106 (2009) 20658–20663.
- [40] W. Man, M. Florescu, K. Matsuyama, P. Yadak, G. Nahal, S. Hashemizad, E. Williamson, P. Steinhardt, S. Torquato, P. Chaikin, Photonic band gap in isotropic hyperuniform disordered solids with low dielectric contrast, *Opt. Express* 21 (2013) 19972–19981.
- [41] G. Gkantounis, T. Amoah, M. Florescu, Hyperuniform disordered phononic structures, *Phys. Rev. B* 95 (2017) 094120.
- [42] M. Salvalaglio, M. Bouabdellaoui, M. Bollani, A. Benali, L. Favre, J.-B. Claude, J. Wenger, P. de Anna, F. Intonti, A. Voigt, M. Abbarchi, Hyperuniform monocrystalline structures by spinodal solid-state dewetting, *Phys. Rev. Lett.* 125 (2020) 126101.
- [43] S. Yu, C.-W. Qiu, Y. Chong, S. Torquato, N. Park, Engineered disorder in photonics, *Nat. Rev. Mater.* 6 (2021) 226–243.
- [44] S. Torquato, D. Chen, Multifunctional hyperuniform cellular networks: optimality, anisotropy and disorder, *Multifunct. Mater.* 1 (2018) 015001.
- [45] J. Kim, S. Torquato, Multifunctional composites for elastic and electromagnetic wave propagation, *Proc. Natl. Acad. Sci.* 117 (2020) 8764–8774.
- [46] J. Kim, S. Torquato, Effective elastic wave characteristics of composite media, *New J. Phys.* 22 (2020) 123050.
- [47] S. Torquato, Extraordinary disordered hyperuniform multifunctional composites, *J. Compos. Mater.* 56 (23) (2022) 3635–3649.
- [48] R. Degl'Innocenti, Y.D. Shah, L. Masini, A. Ronzani, A. Pitanti, Y. Ren, D.S. Jessop, A. Tredicucci, H.E. Beere, D.A. Ritchie, Hyperuniform disordered terahertz quantum cascade laser, *Sci. Rep.* 6 (2016) 19325.
- [49] W. Zhou, Z. Cheng, B. Zhu, X. Sun, H.K. Tsang, Hyperuniform disordered network polarizers, *IEEE J. Sel. Top. Quantum Electron.* 22 (2016) 288–294.
- [50] F. Bigourdan, R. Pierrat, R. Carminati, Enhanced absorption of waves in stealth hyperuniform disordered media, *Opt. Express* 27 (2019) 8666–8682.
- [51] S. Gorsky, W.A. Britton, Y. Chen, J. Montaner, A. Lenef, M. Raukas, L. Dal Negro, Engineered hyperuniformity for directional light extraction, *APL Photonics* 4 (2019) 110801.
- [52] A. Sheremet, R. Pierrat, R. Carminati, Absorption of scalar waves in correlated disordered media and its maximization using stealth hyperuniformity, *Phys. Rev. A* 101 (2020) 053829.
- [53] R. Lin, V. Mazzone, N. Alfaraç, J. Liu, X. Li, A. Fratalocchi, On-chip hyperuniform lasers for controllable transitions in disordered systems, *Laser Photonics Rev.* 14 (2) 1800296.
- [54] Y. Zheng, L. Liu, H. Nan, Z.-X. Shen, G. Zhang, D. Chen, L. He, W. Xu, M. Chen, Y. Jiao, H. Zhuang, Disordered hyperuniformity in two-dimensional amorphous silica, *Sci. Adv.* 6 (2020) eaba0826.
- [55] G. Zhang, F.H. Stillinger, S. Torquato, Transport, geometrical and topological properties of stealthy disordered hyperuniform two-phase systems, *J. Chem. Phys.* 145 (2016) 244109.
- [56] D. Chen, S. Torquato, Designing disordered hyperuniform two-phase materials with novel physical properties, *Acta Mater.* 142 (2018) 152–161.
- [57] Y. Xu, S. Chen, P.-E. Chen, W. Xu, Y. Jiao, Microstructure and mechanical properties of hyperuniform heterogeneous materials, *Phys. Rev. E* 96 (2017) 043301.
- [58] P.P. Mitra, P.N. Sen, L.M. Schwartz, P. Le Doussal, Diffusion propagator as a probe of the structure of porous media, *Phys. Rev. Lett.* 68 (1992) 3555.
- [59] P.N. Sen, M.D. Hürlimann, Analysis of nuclear magnetic resonance spin echoes using simple structure factors, *J. Chem. Phys.* 101 (1994) 5423–5430.
- [60] D.S. Novikov, J.H. Jensen, J.A. Helsen, E. Fieremans, Revealing mesoscopic structural universality with diffusion, *Proc. Natl. Acad. Sci.* 111 (2014) 5088–5093.

- [61] C.E. Maher, F.H. Stillinger, S. Torquato, Characterization of void space, large-scale structure, and transport properties of maximally random jammed packings of superballs, *Phys. Rev. Mater.* 6 (2022) 025603.
- [62] H. Wang, S. Torquato, Dynamic measure of hyperuniformity and nonhyperuniformity in heterogeneous media via the diffusion spreadability, *Phys. Rev. A* 17 (2022) 034022.
- [63] D.A. Coker, S. Torquato, J.H. Dunsmuir, Morphology and physical properties of fontainebleau sandstone via a tomographic analysis, *J. Geophys. Res.* 101 (1996) 17497–17506.
- [64] V.J. Napadow, Q. Chen, V. Mai, P.T.C. So, R.J. Gilbert, Quantitative analysis of three-dimensional-resolved fiber architecture in heterogeneous skeletal muscle tissue using NMR and optical imaging methods, *Biophys. J.* 80 (2001) 2968–2975.
- [65] M.J. Blunt, B. Bijeljic, H. Dong, O. Gharbi, S. Iglauer, P. Mostaghimi, A. Paluszny, C. Pentland, Pore-scale imaging and modelling, *Adv. Water Resour.* 51 (2013) 197–216.
- [66] E. Reid, L. Drummy, C. Bouman, G. Buzzard, Multi-resolution data fusion for super resolution imaging, *IEEE Trans. Comput. Imaging* 8 (2022) 81–95.
- [67] P. Debye, H.R. Anderson, H. Brumberger, Scattering by an inhomogeneous solid. II. The correlation function and its applications, *J. Appl. Phys.* 28 (1957) 679–683.
- [68] O.U. Uche, F.H. Stillinger, S. Torquato, Constraints on collective density variables: Two dimensions, *Phys. Rev. E* 70 (2004) 046122.
- [69] S. Torquato, M. Skolnick, J. Kim, Local order metrics for two-phase media across length scales, *J. Phys. A* 55 (27) (2022) 274003.
- [70] S. Torquato, Disordered hyperuniform heterogeneous materials, *J. Phys.: Condens. Matter* 28 (2016) 414012.
- [71] S. Torquato, Structural characterization of many-particle systems on approach to hyperuniform states, *Phys. Rev. E* 103 (2021) 052126.
- [72] H.E. Stanley, *Introduction to Phase Transitions and Critical Phenomena*, Oxford University Press, New York, 1987.
- [73] J.J. Binney, N.J. Dowrick, A.J. Fisher, M.E.J. Newman, *The Theory of Critical Phenomena: An Introduction to the Renormalization Group*, Oxford University Press, Oxford, England, 1992.
- [74] B.B. Mandelbrot, *The Fractal Geometry of Nature*, W. H. Freeman, New York, 1982.
- [75] S. Torquato, J. Kim, M.A. Klatt, Local number fluctuations in hyperuniform and nonhyperuniform systems: Higher-order moments and distribution functions, *Phys. Rev. X* 11 (2021) 021028.
- [76] E.C. Ögüz, J.E.S. Socolar, P.J. Steinhardt, S. Torquato, Hyperuniformity and anti-hyperuniformity in one-dimensional substitution tilings, *Acta Crystallogr. Sect. A* 75 (2019) 3–13.
- [77] J. Kim, S. Torquato, Characterizing the hyperuniformity of ordered and disordered two-phase media, *Phys. Rev. E* 103 (2021) 012123.
- [78] C.L.Y. Yeong, S. Torquato, Reconstructing random media, *Phys. Rev. E* 57 (1998) 495–506.
- [79] Z. Ma, S. Torquato, Generation and structural characterization of Debye random media, *Phys. Rev. E* 102 (2020) 043310.
- [80] D. Stoyan, W.S. Kendall, J. Mecke, *Stochastic Geometry and its Applications*, second ed., Wiley, New York, 1995.
- [81] Y. Jiao, F.H. Stillinger, S. Torquato, Modeling heterogeneous materials via two-point correlation functions: Basic principles, *Phys. Rev. E* 76 (2007) 031110.
- [82] S. Torquato, Predicting transport characteristics of hyperuniform porous media via rigorous microstructure–property relations, *Adv. Water Resour.* 140 (2020) 103565.
- [83] M. Skolnick, S. Torquato, Understanding degeneracy of two-point correlation functions via Debye random media, *Phys. Rev. E* 104 (2021) 045306.
- [84] C.L.Y. Yeong, S. Torquato, Reconstructing random media: II. Three-dimensional media from two-dimensional cuts, *Phys. Rev. E* 58 (1998) 224–233.
- [85] N.F. Berk, Scattering properties of the leveled-wave model of random morphologies, *Phys. Rev. A* 44 (1991) 5069–5079.
- [86] P.A. Crossley, L.M. Schwartz, J.R. Banavar, Image-based models of porous media—Application to vycor glass and carbonate rocks, *Appl. Phys. Lett.* 59 (1991) 3553–3555.
- [87] A.P. Roberts, M. Teubner, Transport properties of heterogeneous materials derived from Gaussian random fields: Bounds and simulation, *Phys. Rev. E* 51 (1995) 4141–4154.
- [88] A.P. Roberts, Morphology and thermal conductivity of model organic aerogels, *Phys. Rev. E* 55 (1997) R1286–R1289.
- [89] A. Lang, J. Potthoff, Fast simulation of gaussian random fields, *Monte Carlo Methods Appl.* 17 (3) 195–214.
- [90] S. Torquato, Hyperuniformity and its generalizations, *Phys. Rev. E* 94 (2016) 022122.
- [91] Z. Ma, S. Torquato, Random scalar fields and hyperuniformity, *J. Appl. Phys.* 121 (2017) 244904.
- [92] A.M. Dykhne, Conductivity of a two-dimensional two-phase system, *Sov. Phys. JETP* 32 (1971) 63–65.
- [93] S. Torquato, G. Stell, Microstructure of two-phase random media: III. The n -point matrix probability functions for fully penetrable spheres, *J. Chem. Phys.* 79 (1983) 1505–1510.
- [94] S. Torquato, G. Stell, Microstructure of two-phase random media: IV. Expected surface area of a dispersion of penetrable spheres and its characteristic function, *J. Chem. Phys.* 80 (1984) 878–880.
- [95] B. Widom, Random sequential addition of hard spheres to a volume, *J. Chem. Phys.* 44 (1966) 3888–3894.
- [96] G. Zhang, S. Torquato, Precise algorithm to generate random sequential addition of hard hyperspheres at saturation, *Phys. Rev. E* 88 (2013) 053312.
- [97] G. Zhang, F.H. Stillinger, S. Torquato, The perfect glass paradigm: Disordered hyperuniform glasses down to absolute zero, *Sci. Rep.* 6 (2016) 36963.
- [98] G. Zhang, F.H. Stillinger, S. Torquato, Classical many-particle systems with unique disordered ground states, *Phys. Rev. E* 96 (2017) 042146.
- [99] H. Wang, S. Torquato, Equilibrium states corresponding to targeted hyperuniform nonequilibrium pair statistics, *Soft Matter* (2022).
- [100] M. Klatt, P. Steinhardt, S. Torquato, Wave propagation and band tails of two-dimensional disordered systems in the thermodynamic limit, *Proc. Natl. Acad. Sci.* 119 (52) (2022) e2213633119.
- [101] G. Zhang, F.H. Stillinger, S. Torquato, Can exotic disordered stealthy particle configurations tolerate arbitrarily large holes? *Soft Matter* 13 (2017) 6197–6207.
- [102] S. Ghosh, J.L. Lebowitz, Generalized stealthy hyperuniform processes: Maximal rigidity and the bounded holes conjecture, *Comm. Math. Phys.* 363 (2018) 97–110.
- [103] J. McCarthy, Effective permeability of sandstone-shale reservoirs by a random walk method, *J. Phys. A: Math. Gen.* 23 (9) (1990) L445.
- [104] J. McCarthy, Effective conductivity of many-component composites by a random walk method, *J. Phys. A: Math. Gen.* 23 (15) (1990) L749.
- [105] Y. Jiao, F.H. Stillinger, S. Torquato, A superior descriptor of random textures and its predictive capacity, *Proc. Natl. Acad. Sci.* 106 (2009) 17634–17639.
- [106] S.F.S. Shirazi, S. Gharekhani, M. Mehrali, H. Yarmand, H.S.C. Metselaar, N.A. Kadri, N.A.A. Osman, A review on powder-based additive manufacturing for tissue engineering: selective laser sintering and inkjet 3d printing, *Sci. Tech. Adv. Mater.* 16 (2015) 033502.
- [107] J. Kim, S. Torquato, New tessellation-based procedure to design perfectly hyperuniform disordered dispersions for materials discovery, *Acta Mater.* 168 (2019) 143–151.
- [108] J. Haberkro, F. Scheffold, Fabrication of mesoscale polymeric templates for three-dimensional disordered photonic materials, *Opt. Express* 21 (1) (2013) 1057–1065.
- [109] N. Muller, J. Haberkro, C. Marichy, F. Scheffold, Silicon hyperuniform disordered photonic materials with a pronounced gap in the shortwave infrared, *Adv. Opt. Mater.* 2 (2) (2014) 115–119.
- [110] Y. Jiao, F.H. Stillinger, S. Torquato, Distinctive features arising in maximally random jammed packings of superballs, *Phys. Rev. E* 81 (2010) 041304.
- [111] M.A. Klatt, R.M. Ziff, S. Torquato, Critical pore radius and transport properties of disordered hard-and overlapping-sphere models, *Phys. Rev. E* 104 (2021) 014127.